Journal of Sound and Vibration 333 (2014) 1857–1873

Contents lists available at ScienceDirect

Journal of Sound and Vibration

journal homepage: www.elsevier.com/locate/jsvi

Comparison of various decentralised structural and cavity feedback control strategies for transmitted noise reduction through a double panel structure

Jen-Hsuan Ho [a,*], Arthur Berkhoff [a,b]

[a] Department of Electrical Engineering, University of Twente, P.O. Box 217, 7500 AE Enschede, The Netherlands
[b] TNO Technical Sciences, Acoustics and Sonar Acoustics, P.O. Box 96864, 2509 JG Den Haag, The Netherlands

ARTICLE INFO

Article history:
Received 3 October 2012
Received in revised form
15 September 2013
Accepted 8 November 2013
Handling Editor: J. Lam
Available online 21 December 2013

ABSTRACT

This paper compares various decentralised control strategies, including structural and acoustic actuator–sensor configuration designs, to reduce noise transmission through a double panel structure. The comparison is based on identical control stability indexes. The double panel structure consists of two panels with air in between and offers the advantages of low sound transmission at high frequencies, low heat transmission, and low weight. The double panel structure is widely used, such as in the aerospace and automotive industries. Nevertheless, the resonance of the cavity and the poor sound transmission loss at low frequencies limit the double panel's noise control performance. Applying active structural acoustic control to the panels or active noise control to the cavity has been discussed in many papers. In this paper, the resonances of the panels and the cavity are considered simultaneously to further reduce the transmitted noise through an existing double panel structure. A structural–acoustic coupled model is developed to investigate and compare various structural control and cavity control methods. Numerical analysis and real-time control results show that structural control should be applied to both panels. Three types of cavity control sources are presented and compared. The results indicate that the largest noise reduction is obtained with cavity control by loudspeakers modified to operate as incident pressure sources.

1. Introduction

Traditionally, noise control methods are based on passive noise control, which means applying high damping materials, adding mass, adding resilient elements or installing absorbing resonators in the system. Passive noise control can effectively reduce noise at high frequencies [1,2]. However, there is typically much less noise reduction at low frequencies, and reduction requires a substantial implementation cost because the acoustic wavelengths are much longer than the damping structure [3,4]. Conversely, active noise control offers the potential advantages of decreased weight and better performance at low frequencies. With the development of smart materials and computational power, active noise control has received increasing attention in the past few decades. Traditional active noise control (ANC) for reducing broadband noise has been successfully applied in relatively small spaces [5,6]. However, for a larger control volume, the 3D wave propagation problem causes the control implementation to become too complicated and inefficient. Therefore, active structural acoustic control (ASAC) was

* Corresponding author. Tel.: +31 53 489 2842; fax: +31 53 489 1060.
E-mail addresses: j.ho@utwente.nl (J. Ho), a.p.berkhoff@utwente.nl (A. Berkhoff).

0022-460X/$ - see front matter © 2013 Elsevier Ltd. All rights reserved.
http://dx.doi.org/10.1016/j.jsv.2013.11.018

proposed to simplify the control computation. ASAC can simplify a 3D problem to a 2D problem by directly controlling the vibrating structure to reduce the structure's radiating sound pressure instead of addressing 3D acoustic wave propagation [6,7]. Furthermore, for a large configuration, decentralised control or distributed control can make the controller suitable for practical implementations [8–12]. Moreover, the remarkable performance of the decentralised feedback control strategy for the broadband objective has been observed [13]. A double panel structure, which consists of two panels with air in the gap, is another common implementation for noise reduction. The double panel structure offers the advantages of low sound transmission at high frequencies, low heat transmission, and low weight [1,14–16]. Piezoelectric materials have been investigated and applied frequently for vibration control of smart structures because of the compact dimensions and rapid response of these materials [5,11,17]. In this paper, a double panel structure with multiple decentralised feedback control is investigated. Various structural and cavity control strategies are applied to this system to reduce the amount of noise transmitted. A structural–acoustic coupled model is developed, and the dominant structural/acoustic modes of the double panel structure at resonance frequencies are analysed. The panel control principles in the double panel structure are incorporated in the structural–acoustic model and are validated with a real-time control implementation. Several control strategies based on identical control stability indexes are compared to find the optimal control method, which leads us to further investigate various cavity control strategies. The principal contributions of the present paper are the detailed investigation and comparison of the various decentralised structural and cavity feedback control strategies in double panel structures, all of which are based on identical control stability indexes.

This paper has four main sections. Section 2 describes a multichannel decentralised feedback control system for a fully coupled plant matrix and a method for control stability analysis. Section 3 describes our numerical model and the experiment measurement set-up. Section 4 presents and discusses the detailed investigations of the structural control, cavity control, combination control and comparisons. Section 5 provides a control performance comparison of various cavity control sources.

2. Control method

2.1. Multiple decentralised feedback control

Fig. 1 illustrates the signal block diagram of a feedback control system. $\mathbf{e}(\mathrm{j}\omega)$ is the error signal matrix, where ω is the angular frequency [rad s^{-1}] and $\mathrm{j}=\sqrt{-1}$. $\mathbf{G}(\mathrm{j}\omega)$ is the plant transfer matrix; $\mathbf{u}(\mathrm{j}\omega)$ is the control signal matrix; $\mathbf{d}(\mathrm{j}\omega)$ is the noise source matrix, which is the error signal without the input control signal; and $\mathbf{H}(\mathrm{j}\omega)$ is the control matrix, which is a constant H in this paper. The time-dependent signals are the real part of the complex vectors (i.e., the time-dependent error signal $\mathbf{e}(t)=\mathrm{Re}\{\mathbf{e}(\mathrm{j}\omega)\mathrm{e}^{\mathrm{j}\omega t}\}$).

From the block diagram in Fig. 1, $\mathbf{e}(\mathrm{j}\omega)$ can be derived as

$$\mathbf{e}(\mathrm{j}\omega)=[\mathbf{I}+\mathbf{G}(\mathrm{j}\omega)\mathbf{H}(\mathrm{j}\omega)]^{-1}\mathbf{d}(\mathrm{j}\omega), \tag{1}$$

where $\mathbf{I}$ is an identity matrix. To present the physical interactions between each control unit in a multiple-input and multiple-output (MIMO) control system, a fully coupled multiple channel plant transfer matrix $\mathbf{G}(\mathrm{j}\omega)$ is applied:

$$\mathbf{G}(\mathrm{j}\omega)=\begin{bmatrix}\mathbf{G}_{11}(\mathrm{j}\omega) & \cdots & \mathbf{G}_{1m}(\mathrm{j}\omega)\\ \vdots & \ddots & \vdots\\ \mathbf{G}_{l1}(\mathrm{j}\omega) & \cdots & \mathbf{G}_{lm}(\mathrm{j}\omega)\end{bmatrix}, \tag{2}$$

where $\mathbf{G}_{lm}(\mathrm{j}\omega)$ is the transfer matrix from the m-th actuator to the l-th sensor.

2.2. Control stability

In theory, the stability of a feedback control system can be unconditionally guaranteed when the sensors and actuators are dual and collocated [18]. Therefore, the control gain can be increased infinitely to decrease the error signals of Eq. (1) to

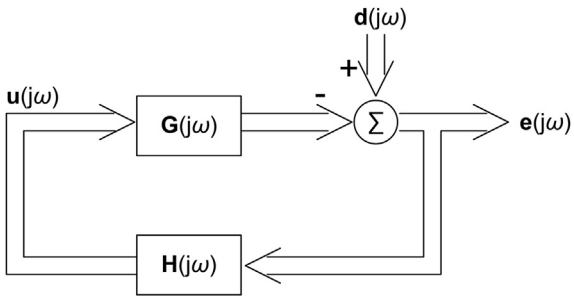

Fig. 1. Direct velocity feedback systems.

zero. To determine the stability of practical MIMO decentralised control systems, the generalised Nyquist criterion can be applied [13]. The system is stable if and only if the locus of det[$\mathbf{I}+\mathbf{G}(j\omega)\mathbf{H}(j\omega)$] does not cross or encircle the origin (0, 0). However, a stable system can become unstable in the presence of perturbations. The ability of the system to withstand perturbations is defined by stability margins in a single-input and single-output (SISO) control system. On the other hand, in an MIMO system, even a simultaneous change in the gain or phase in all of the loops may change the shape of the locus of det[$\mathbf{I}+\mathbf{G}(j\omega)\mathbf{H}(j\omega)$]. Therefore, the margins of the locus of det[$\mathbf{I}+\mathbf{G}(j\omega)\mathbf{H}(j\omega)$] give different meanings to the classical definitions. One method to access the classical stability margins in an MIMO system is to use the eigenvalue loci. The eigenvalue loci are the eigenvalues of the frequency response of $\mathbf{G}(j\omega)\mathbf{H}(j\omega)$, which can provide Nyquist plots with the classically defined margins. Nevertheless, these margins are not practically useful since the system is assumed to have a simultaneous and identical change in the gain or phase in all of the loops [19]. Another method is to first analyse each individual control loop to govern the stability margins of each single channel. The stability margins of the single channel present the physics and intrinsic limitations of the sensor–actuator feedback loop. And the maximum control gain of each individual control unit can be found. However, the margins from this analysis cannot guarantee the mutual stability of the multiple control units. Therefore, the next step is to apply the generalised Nyquist stability criterion to prove the stability of the multiple feedback control system with the maximum mutual control gain, which is smaller than the maximum single channel control gains from each individual control units [15,20]. Since the main purpose of this paper is to compare the noise reduction of various control strategies, simple but relatively fair stability criteria are applied in this paper. The gain stability index, phase stability index, and modulus stability index in an MIMO system are defined as the stability margins of the locus of det[$\mathbf{I}+\mathbf{G}(j\omega)\mathbf{H}(j\omega)$]. Although these indexes are different to the classical margins in an SISO system, they can provide us the approximations of control stability margins.

3. Numerical model and experiment set-up

This section describes our noise reduction analysis method. First, the numerical model, including both acoustic and structural characteristics, is introduced. Then, the experiment set-up and the method for estimating radiated sound based on vibration measurements are described. The final part provides the model validation.

3.1. Structural–acoustic interaction FEM model

We use the finite element method (FEM) with the COMSOL Multiphysics 4.2 (COMSOL, Inc., Burlington, MA 01803, USA) to model and analyse the characteristics of our system. To accurately model the system, the acoustic and structural properties must be considered simultaneously. Moreover, the interactions between the properties should be applied to both sides to achieve a more accurate result. Therefore, there are two domains in our model: the fluid domain and the solid domain. The relationship of the acoustic pressure in the fluid domain to the structural deformation in the solid domain is linked as described below. In the solid domain, the normal force to the structure $\mathbf{F}_p$ [N] produced by the fluid pressure p [Pa] on the fluid–solid interacting boundaries is given by

$$\mathbf{F}_p = -\mathbf{n}\cdot p, \tag{3}$$

where $\mathbf{n}$ is the normal vector of the solid boundaries. In the acoustic fluid domain, the normal acceleration to the acoustic pressure a_n [m s^{-2}] on the fluid–solid interacting boundaries can be derived from the second derivatives of the structural displacements with respect to time $\mathbf{u}_{tt}$ [m s^{-2}]:

$$a_n = \mathbf{n}\cdot\mathbf{u}_{tt}. \tag{4}$$

By applying Eqs. (3) and (4), the interaction between the acoustic field and solid structure can be investigated.

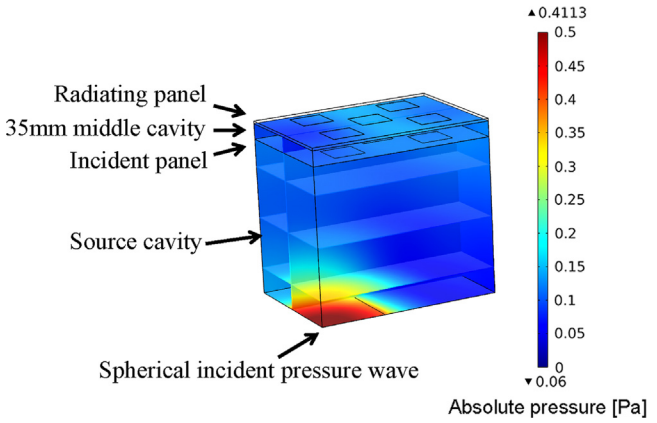

Fig. 2. Structural–acoustic interaction model.

3.2. Model configuration and experiment set-up

The resonant behaviour and sound transmission of a double panel structure are investigated based on the model shown in Fig. 2. A spherical incident pressure wave acts as the primary noise source. To produce an asymmetrical incident noise wave, this wave is generated from the bottom corner of the source cavity. This primary noise source from the source cavity first enters an aluminium panel (the incident panel), then a 35 mm-thick layer of air (the middle cavity), followed by a honeycomb panel (the radiating panel). These two panels are simply supported. Furthermore, high absorbing materials are applied to the surface of the source cavity to reduce the resonant energy from the source cavity. The detailed model parameters are provided in Table 1.

The energy of the near field sound pressure wave is related to the kinetic energy of the radiating panel at lower modes [21]. Fig. 3 shows the near field sound pressure wave from the radiating panel of the double panel structure. Directly calculating the near field sound pressure requires more computation than calculating the kinetic energy of the radiating panel. Therefore, to analyse the control performance of various control strategies, we use the kinetic energy of the radiating panel to represent the near field sound. Although the surface mass density affects the ratio of the kinetic energy of the radiating panel to the radiating sound pressure above the radiating panel, all the kinetic energy frequency responses in this paper are obtained from the same honeycomb material, which means the ratio is fixed. Moreover, this paper presents the transmitted noise reduction comparison of various control strategies applied to the same double panel structure. We

Table 1
Model parameters.

	Parameters	Values	Unit
Aluminium panel (incident panel)	Dimensions		
	1. Validation model	420*297*1	[mm^3]
	2. Controlled analysis model	420*297*2	[mm^3]
	Density	2700	[$kg\ m^{-3}$]
	Young's modulus	70	[GPa]
	Poisson's ratio	0.33	
	Loss factor	0.03	
Honeycomb panel(radiating panel)	Dimensions	420*297*5.8	[mm^3]
	Density	409	[$kg\ m^{-3}$]
	Young's modulus	3.7	[GPa]
	Poisson's ratio	0.33	
	Loss factor	0.03	
Piezoelectric patches	Dimensions	72.4*72.4*0.264	[mm^3]
	Density	7800	[$kg\ m^{-3}$]
	Young's modulus	52	[GPa]
	Poisson's ratio	0.33	
	Strain coefficient d_{31}	-190	[$m\ V^{-1}$]
Source cavity	Inner dimensions	420*297*350	[mm^3]
	High absorbing surface, acoustic impedance	1000	[$Pa\ s\ m^{-1}$]
Middle cavity	Inner dimensions	420*297*35	[mm^3]
	Rigid boundary		

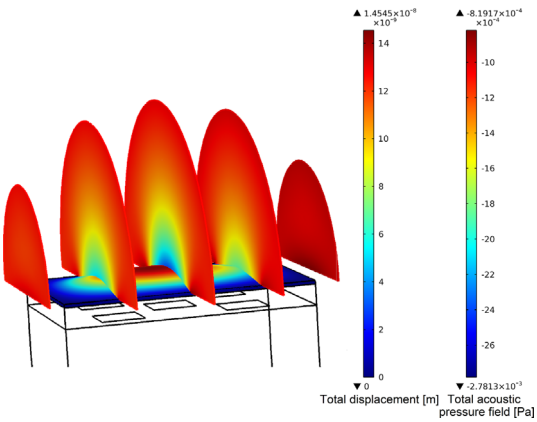

Fig. 3. Near field sound pressure wave from the radiating panel.

compared the structure's near-field sound pressure, which can be represented by the kinetic energy of the radiating panel. Therefore, the far-field radiation efficiency of the radiating panel does not affect the comparison results in this paper. However, to fully present the controlled results of various control methods, the sound pressure level at 10 cm above the radiating panel surface and the radiated sound power level of the radiating panel are given in Sections 4.4 and 5.4.

Fig. 4(a) shows our experiment set-up. The double panel is mounted on a rectangular box, which is referred to as the source cavity. A loudspeaker at the bottom of the rectangular box generated the primary noise. The kinetic energy of the radiating panel can be derived by measuring the velocity of this panel. The structural control sets on the radiating panel (five piezoelectric actuators and five acceleration sensors) are shown in Fig. 4(b). Furthermore, this box was constructed with 40 mm-thick walls of acrylic plates to prevent the sound from leaking through the side walls. Although we provide only the kinetic energy results in this paper, the transmitted sound was also measured by locating a microphone above the top panel.

3.3. Kinetic energy estimation

As mentioned above, we used the kinetic energy of the radiating panel to represent the near field sound pressure from the panel. The measured kinetic energy of the panel was derived from the sensors on the panel. These sensors were equally distributed on the panel. We used the average velocity of these sensor points to calculate the kinetic energy of the panel. Therefore, more sensor points can improve the accuracy of the kinetic energy estimate, particularly for the higher vibration modes. However, in practice, the number of detecting sensors is limited. The required number of sensors depends on the mode shape complexity of the panel. To guarantee the accuracy of our kinetic energy estimate and to avoid estimation errors because of an insufficient number of sensors, we first compared the accuracy of various sensor numbers using the FEM model. A panel was excited by an incident acoustic wave, and the kinetic energy estimates for this panel from 1, 2, 4, 5, 9, 16, and 25 velocity sensor points were compared with the integral kinetic energy of the entire panel. To provide an accurate approximation of the panel response, the distance between two adjacent monitoring positions should be smaller than half a bending wavelength of the panel. The bending wave speed of the radiating panel was 259 m s^{-1} and the half bending wavelength of the panel was 6.5 cm at the maximum frequency 2 kHz. The panel model was divided up into 1718 elements and the distance between two adjacent positions was less than 15 mm, which is smaller than half bending wavelength of the panel. Fig. 5 shows the kinetic energy frequency response of the panel from 10 Hz to 2000 Hz.

At each frequency, the error is the absolute difference in dB between the estimated kinetic energy and real kinetic energy. We average all of these errors to obtain the estimation error, which is shown in Table 2 for the various sensor results. These results show that using only one sensor on the panel is insufficient for obtaining a correct estimate because a single sensor cannot present the characteristics of any mode shape that is higher than the first mode, such as (2, 1), (1, 2), and (2, 2). However, below 1000 Hz, the estimated kinetic energy from 5 and 9 velocity sensor points can precisely match the integral kinetic energy. Therefore, we can use the average velocity from 5 or 9 sensors to estimate the kinetic energy of the entire panel. In our model validation, the measured kinetic energy was derived from 9 sensors on the panel. In our real-time

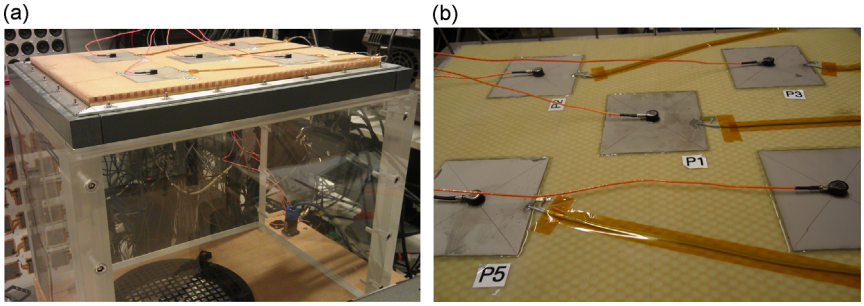

Fig. 4. (a) Experiment set-up for real-time control; (b) five actuator–sensor pairs on the radiating panel.

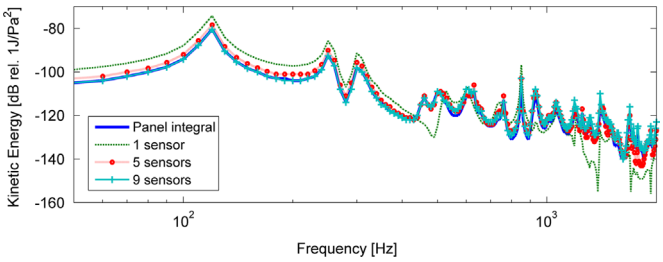

Fig. 5. Kinetic energy numerical analysis of the radiating panel derived from different numbers of sensor points.

Table 2
Kinetic energy difference.

Average difference of kinetic energy [dB] (Average(abs(10*log 10(ΣKE_sensors/ΣKE_panel integral))))							
Sensor number(s)	1	2	4	5	9	16	25
10–500 Hz	6.622	3.982	0.989	1.739	0.145	0.017	0.030
10–1000 Hz	6.064	4.810	1.500	2.037	1.073	0.200	0.059
10–2000 Hz	7.121	5.512	2.157	2.277	1.879	0.884	0.513

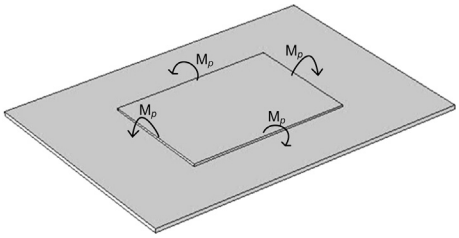

Fig. 6. Four line moments representing the equivalent piezoelectric load for a laminar piezoelectric actuator.

control, we used 5 sensors, which were the error sensors in the feedback control loop, to derive the kinetic energy of the panel.

3.4. Equivalent piezoelectric load

In this paper, piezoelectric patches are applied for the structural control. Piezoelectric materials offer the advantages of rapid response and compact dimensions. The equivalent piezoelectric load equation for laminar piezoelectric actuators is adopted to simplify the model, where the piezoelectric force can be represented as line moments on the edges of the piezoelectric patch shown in Fig. 6 [22]. The line moment is given by

$$M_p = -E_p d_{31} h V, \tag{5}$$

where M_p [N] is the moment per unit length, E_p [GPa] is the Young's modulus of the piezoelectric patch, d_{31} [m V^{-1}] is the piezoelectric strain coefficient, h [m] is the distance between the mid-plane of the piezoelectric patch and the mid-plane of the panel, and V [V] is the control voltage applied to the patch. In our numerical analysis, the control force from each piezoelectric patch is applied as four line moments on the panel.

3.5. Model validation

To validate our numerical model, a kinetic energy response comparison between the simulation and experiment was performed. We used the kinetic energy response of the radiating panel, whereas there was an excitation force on the radiating panel (the honeycomb panel). Fig. 7 shows the experiment set-up for our model validation. One piezoelectric patch was attached to the honeycomb panel to apply the excitation force.

Then, we measured the acceleration of the panel from nine positions to derive the panel's kinetic energy, which is based on the panel integration of the acceleration, and compared the result with that from the numerical simulation, as shown in Fig. 8(a). The figure shows that the numerical model can accurately predict the practical sensor–actuator response in a single panel structure. To further validate the double panel interaction result, we added another panel below the radiating panel with a 35 mm air gap to change the structure into a double panel structure. This second panel was a 1 mm-thick aluminium panel, which has a high resonance density. The excitation force was only applied on the radiating panel. Fig. 8(b) shows that the number of resonant peaks of the double panel structure increases because of the resonance contributions from the incident panel and cavity. However, the numerical model can estimate the practical sensor–actuator response in a double panel structure with reasonable error. The 1 mm-thick aluminium panel with a high resonance density was chosen to obtain a more complex response object to compare with our numerical model. However, because of the concern for control stability, instead of the 1 mm-thick aluminium panel, a 2 mm-thick aluminium panel was attached to the double panel structure for subsequent analysis and experiments.

4. Control performance and discussion

In this section, we present the results of applying structural control, cavity control, and structural-cavity combination control to the double panel structure. First, we used piezoelectric patches on the incident panel and radiating panel to control the structure. The limitation of the structural control was analysed, and the real-time structural control was measured to prove our conclusion from the numerical analysis. Next, we analysed the cavity control using traditional

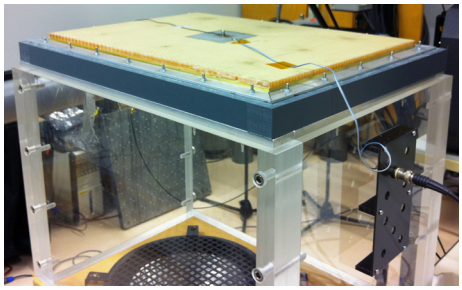

Fig. 7. Validation experiment set-up.

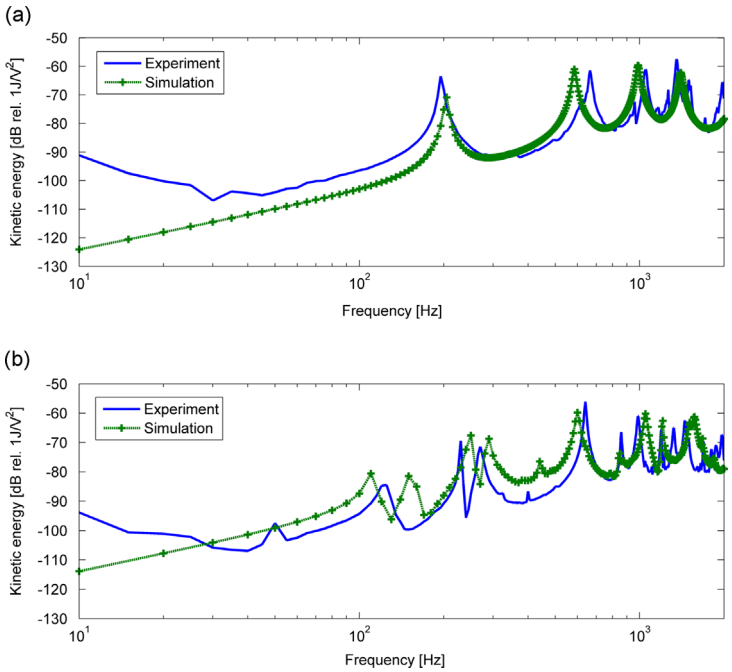

Fig. 8. Experimental and simulated kinetic energy response of the radiating panel: (a) the single panel structure; (b) the double panel structure.

loudspeakers as the cavity sources. Finally, we combined the two methods, which is referred to as the structural-cavity combination control, and compared the various control methods to find the most effective strategy to reduce the transmitted noise.

4.1. Control configurations

Two simply supported panels with a 35 mm-thick air gap comprised the double panel structure. The incident panel was a 2 mm-thick aluminium panel, and the radiating panel was a 5.8 mm-thick honeycomb panel. The parameter details are listed in Table 1. In the structural control case, as described in Section 4.2, an analysis is given of five piezoelectric patches attached to each panel (Fig. 9). On each piezoelectric patch, there is one collocated acceleration sensor that functions as the error sensor for the velocity feedback control system.

In the cavity control case, as described in Section 4.3, an analysis is given of six loudspeakers installed in the cavity between these double panels (Fig. 10). In front of each loudspeaker, there is one microphone that functions as the error sensor for the feedback control system. The microphone positions are the circles marked with red in Fig. 10.

4.2. Structural control

First, we numerically analysed the stability, frequency response and resonant modes of the structure-controlled system. Then, the real-time control was performed to support the conclusions from the numerical analysis.

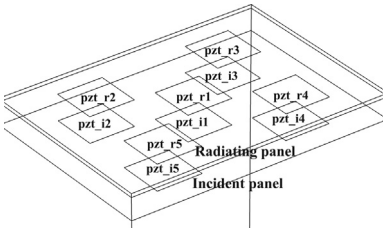

Fig. 9. Control sets on the panels.

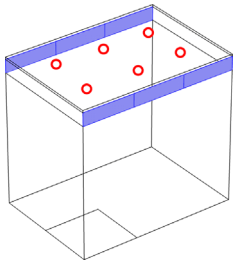

Fig. 10. Distribution of control sets for cavity control. (For interpretation of the references to colour in this figure legend, the reader is referred to the web version of this article.)

4.2.1. Numerical structural control analysis

Table 3 lists the Nyquist plots for the following structure-controlled cases. Since the accelerometer and the piezoelectric patch were neither dual nor collocated, the feedback loop was not unconditionally stable. The system therefore included a low-pass filter with a cut-off frequency of 1000 Hz to prevent instability at higher frequencies. Zoomed figures around the origin are listed in the table to confirm the system stability. In the first and second plots, only the incident panel was controlled with control gain 800. In the third and fourth plots, only the radiating panel was controlled with control gain 330. The plots show that with the low-pass filter, the stability was improved at higher frequencies. Moreover, because these plots do not encircle or cross the origins, the stability of the system is guaranteed.

The control performance of these two cases without and with the low-pass filter is shown in Figs. 11 and 12. Fig. 12. shows that the low-pass filter does not weaken the control performance. Moreover, although controlling the radiating panel can effectively reduce the near field sound in a single panel structure, it cannot reduce all of the resonant peaks in a double panel structure. For instance, for the first few resonant peaks, only the second and fourth peaks can be reduced by controlling the radiating panel. However, the first and third peaks were barely reduced. In contrast, the first and third peaks can be significantly reduced by controlling the incident panel, but the second and fourth peaks were barely reduced.

Furthermore, in the double panel structure, there is a major drop of the sound transmission-loss, where the sound transmission-loss can even be less than that of a single panel structure. This particular frequency is referred to as the mass–air–mass frequency, where the two panels have anti-phase motion and the air acts as a spring [4]. The calculated mass–air–mass resonant frequency for unbounded panels is 256 Hz in this case, while the resonant frequency at 250 Hz is shown in our FEM simulation result. To further describe the difference, the uncontrolled resonant mode shapes of the panels and the uncontrolled acoustic pressure distribution in the cavity are shown in Table 4. The mode shapes show that the first and third resonance frequencies are dominated by the resonant modes of the incident panel. Conversely, the second and fourth resonance frequencies mainly result from the radiating panel. Furthermore, the fifth resonant peak at 500 Hz is dominated by the acoustic resonance of the cavity. Table 5 shows the mode shapes of the radiating panel with various structural control methods. From these results, we can observe that the peaks that are dominated by the incident panel resonant modes (120 Hz and 300 Hz) can be effectively reduced by applying the incident-panel piezoelectric actuators. In contrast, the peaks that are dominated by the radiating panel resonant modes (250 Hz and 460 Hz) can be effectively reduced by applying the radiating-panel piezoelectric actuators. Thus, all the structure-dominated resonant peaks can be reduced when the radiating panel and incident panel are controlled, as shown in the last row of Table 5. The control gain for both controlled-panel cases should be readjusted to ensure the stability of the system. The Nyquist plot is shown in Table 6, where the control gains for the incident panel and radiating were 500 and 300, respectively. In the second plot, the low-pass filter was applied. Fig. 13 shows the control performance when both panels were controlled and shows the low-pass filter does not weaken the control performance. Although all of the structure-dominated resonant peaks can be reduced, the size of this reduction decreased. Because of the interference between these two panels, the control gain of both panels was limited. Therefore, the reduction of these resonant peaks was limited. Furthermore, the result shows that although controlling the two panels can reduce most of the resonant peaks, which also include the mass–air–mass resonant frequency, it can barely reduce the resonant peak at the cavity-dominated resonant frequency (500 Hz).

Table 3
Numerical analysis of panel control positions, locus of det[$\mathbf{I}+\mathbf{G}(j\omega)\mathbf{H}(j\omega)$] from 10 to 20,000 Hz: from 10 to 1000 Hz (blue solid lines) and from 1000 to 20,000 Hz (green dotted lines).

Control position	Locus of det[$\mathbf{I}+\mathbf{G}(j\omega)\mathbf{H}(j\omega)$]	Zoomed around (0, 0)
Incident panel	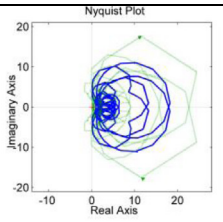	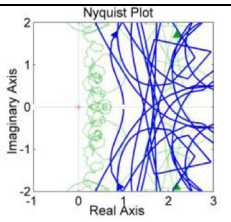
Incident panel with the low-pass filter	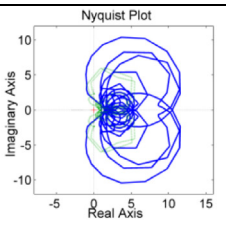	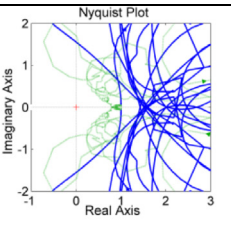
Radiating panel	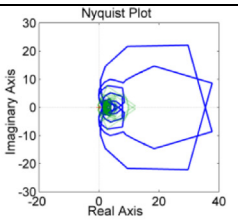	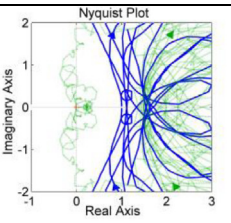
Radiating panel with the low-pass filter	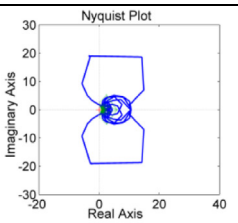	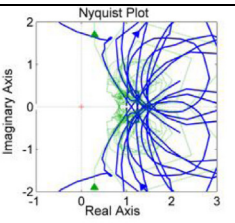

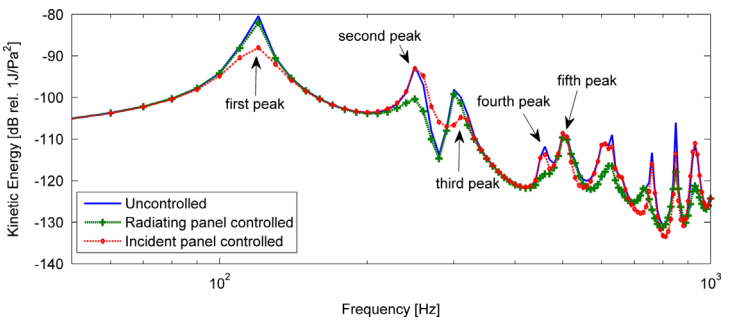

Fig. 11. Simulated kinetic energy response of the radiating panel with panel control.

4.2.2. Real-time structural control

To further support the conclusions of the numerical analysis, a real-time structural control measurement was performed. First, we applied the structural control to a single panel structure, whereby five piezoelectric actuators were attached to the panel. The excitation noise source was the acoustic pressure produced by a loudspeaker. The control result indicated that the structural control could effectively reduce the resonant energy in the single panel structure (Fig. 14(a)). Next, we added a second panel (the incident panel) under the first panel (the radiating panel) with an air layer between the panels to change the system into a double panel structure. The structural control was only applied to the radiating panel, and the control

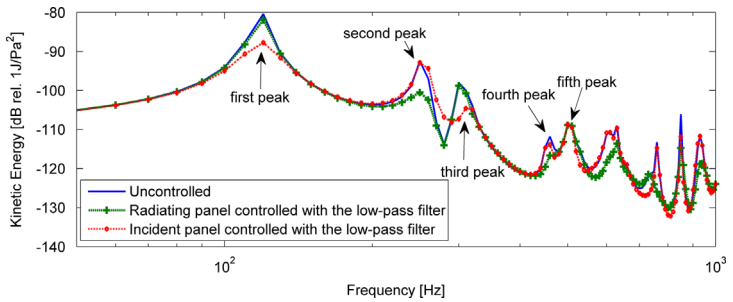

Fig. 12. Simulated kinetic energy response of the radiating panel with low-pass filtered panel control.

Table 4
Simulated mode shapes of the uncontrolled system.

Frequency [Hz]	120	250	300	460	500
Displacement mode shapes	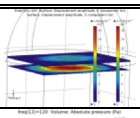	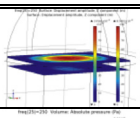	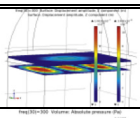	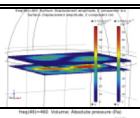	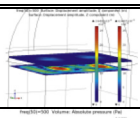
Absolute pressure distribution	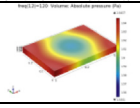	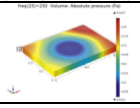	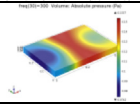	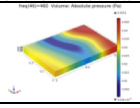	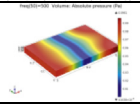

Table 5
Simulated mode shapes of the radiating panel with various structural control methods.

Frequency [Hz]	120	250	300	460
Uncontrolled	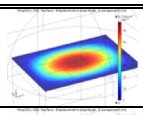	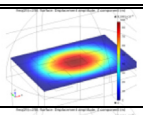	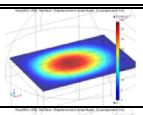	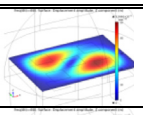
Incident panel controlled	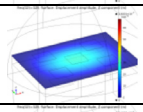	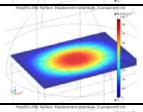	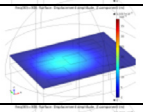	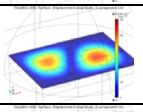
Radiating panel controlled	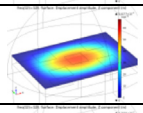	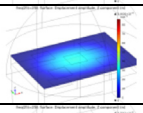	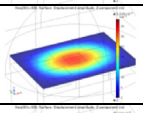	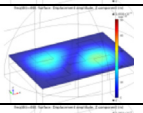
Both panels controlled	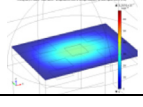	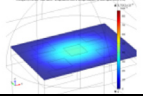	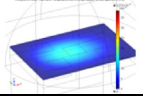	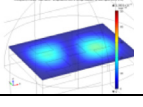

result is shown in Fig. 14(b). The figure shows that controlling only the radiating panel in a double panel structure can only reduce certain peaks instead of all the resonant peaks because these resonant peaks were not only determined by the resonant modes of the incident panel. This result agreed with our numerical analysis.

The resonance frequencies of a double panel structure result from not only the radiating panel but also the incident panel. Therefore, both panels should be controlled simultaneously in a double panel structure. Nevertheless, resonant energy also emerges from the cavity, such as the frequency at 500 Hz. This resonant energy can be barely reduced by adding active damping to the structure. This limitation of the structural control should be considered in the system design.

4.3. Cavity control

The previous section has shown that applying direct velocity feedback control to the structure cannot effectively control the cavity-dominated resonance in a double panel structure. To solve this problem, six decentralised cavity controllers were modelled in the middle cavity between the double panels. In each controller, one pressure sensor was assumed in the cavity

Table 6
Numerical analysis of both panels controlled, locus of det[$\mathbf{I}+\mathbf{G}(j\omega)\mathbf{H}(j\omega)$] from 10 to 20,000 Hz: from 10 to 1000 Hz (blue solid lines) and from 1000 to 20,000 Hz (green dotted lines).

	Locus of det$[\mathbf{I}+\mathbf{G}(j\omega)\mathbf{H}(j\omega)]$	Zoomed around (0, 0)
Both panels controlled	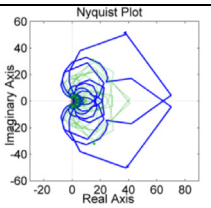	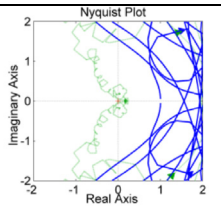
Both panels controlled with the low-pass filter	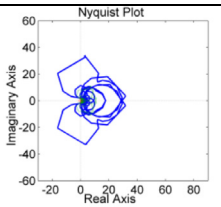	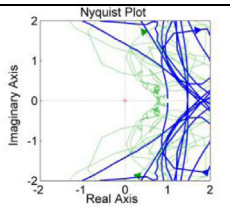

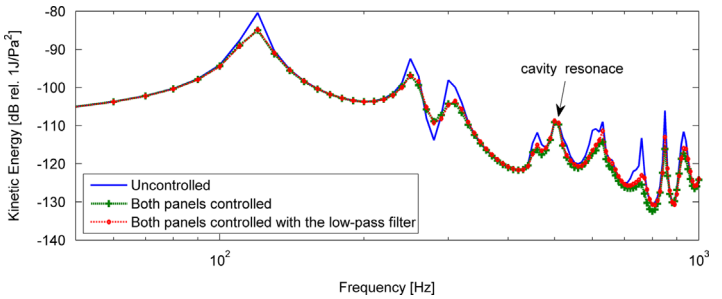

Fig. 13. Simulated kinetic energy response of the radiating panel with both panels controlled.

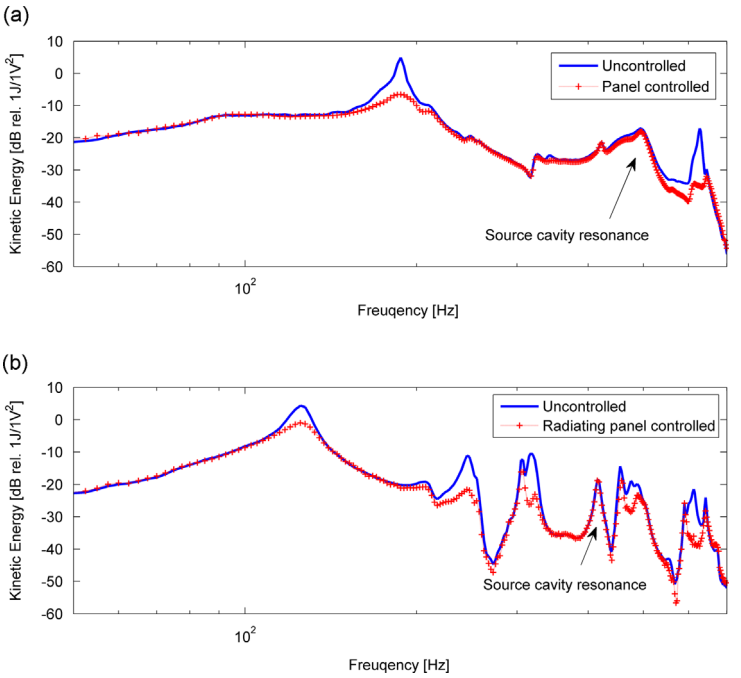

Fig. 14. Experimental kinetic energy response of the radiating panel: (a) single panel control result; (b) double panel control result.

and one loudspeaker to produce the secondary control source. The loudspeaker was a dynamic loudspeaker and thus assumed to operate as an acceleration source above the resonance frequency. The Nyquist plot of this MIMO decentralised control system with a control gain of 0.0003 is shown in Table 7. In the second plot, a low-pass filter with a cut-off frequency of 1000 Hz to prevent instability at higher frequencies was applied to the control system. The locus of det[$\mathbf{I}+\mathbf{G}(j\omega)\mathbf{H}(j\omega)$] does not encircle or cross the origin, which guarantees the stability of the control system.

Fig. 15 shows the control performance without and with the low-pass filter and shows the low-pass filter does not weaken the control performance. With the cavity control, the kinetic energy can be reduced not only at the structure resonance-dominated frequencies but also at the cavity resonance-dominated frequencies. The result shows that cavity control can provide significant transmitted noise. Therefore, cavity control strategies were further investigated, as discussed in Section 5.

4.4. Combined control and comparisons

To improve the control performance, we applied structural control and cavity control to the system simultaneously, which is referred to as structural-cavity combination control. The stability was guaranteed with a fully coupled plant transfer matrix, in which 16 actuators and 16 sensors were simultaneously considered. All the open loop frequency response functions are computed above the crossover frequency, and every Nyquist plot does not cross or encircle the origin (0,0). In addition, we compared the control performance of the structural control, cavity control, and combination control based on identical stability indexes. The gain stability index, phase stability index, and modulus stability index in Table 8 are defined as the stability margins of the locus of det[$\mathbf{I}+\mathbf{G}(j\omega)\mathbf{H}(j\omega)$] from 10 Hz to 1000 Hz. An infinity gain margin index means the smallest value at the x-axis of the locus of det[$\mathbf{I}+\mathbf{G}(j\omega)\mathbf{H}(j\omega)$] from 10 Hz to 1000 Hz is large than 1. Although the margin indexes from the full frequency spectrum should be considered, since the instability is caused at higher frequencies in

Table 7
Numerical analysis of cavity control, locus of det[$\mathbf{I}+\mathbf{G}(j\omega)\mathbf{H}(j\omega)$] from 10 to 20,000 Hz: from 10 to 1000 Hz (blue solid lines) and from 1000 to 20,000 Hz (green dotted lines).

	Locus of det[$\mathbf{I}+\mathbf{G}(j\omega)\mathbf{H}(j\omega)$]	Zoomed around (0, 0)
Cavity controlled	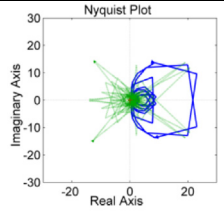	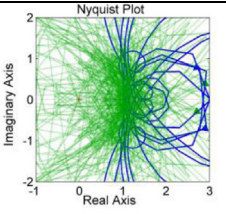
Cavity controlled with the low-pass filter	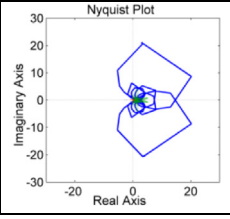	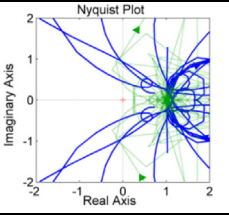

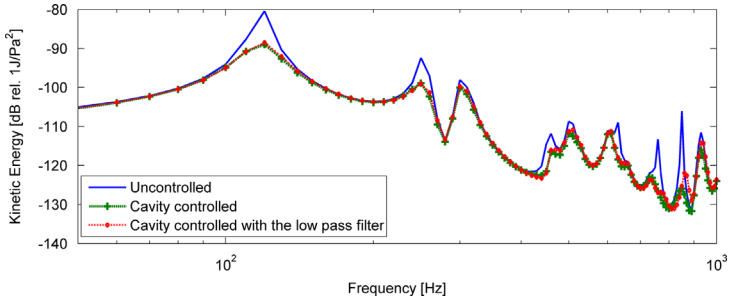

Fig. 15. Simulated kinetic energy response of the radiating panel with cavity control.

practical applications, the stability at higher frequencies can be improved. For example, decreasing the distance between the loudspeaker and the microphone can improve the stability because the phase lag caused by the distance between the sensor and the actuator is decreased substantially, particularly at higher frequencies. Furthermore, the phase crossover frequency, which happens above 1000 Hz, of the system is given to provide a complete view of the system. The controlled results are presented in three plots: the kinetic energy of the radiating panel, the sound pressure level (SPL) at 10 cm above the radiating panel and the radiating sound power level (SWL) of the radiating panel (Figs. 16–18). Moreover, we calculated the total kinetic energy reduction and the total radiated sound power reduction of each control method from 10 Hz to 1000 Hz to provide a clearer index of the noise reduction (Table 8). The table shows that applying cavity control can reduce more of the radiating panel's kinetic energy and the total radiated sound power than the other two methods. Although the combination control method controls both the structure and cavity, the control gain is limited because of the stability constraint. Therefore, the combination control method cannot provide more noise reduction than the cavity control method.

Table 8
Numerical analysis of stabilities, kinetic energy reduction and radiated sound power reduction from 10 to 1000 Hz.

Combinations	6 loudspeakers (acc. source*)	10 pzt (inc. & rad. panel*)	6 Loudspeakers (acc. source) & 10 pzt (inc. & rad. panel)
Control gain	0.00042	350 (inc.); 150 (rad.)	0.00021 (lsp); 300 (inc.); 125 (rad)
Gain stability index	Inf.	Inf.	Inf.
Phase stability index	58.7	60.7	−61.0
Modulus stability index	0.87	0.98	0.96
Phase crossover frequency [10–20,000 Hz]	10,033	8841	7818
Total kinetic energy reduction (10*log 10(ΣKE_uncontrolled/ΣKE_controlled)) [dB]			
	4.9	2.9	4.6
Total radiated sound power reduction (10*log 10(Σradiated_power_uncontrolled/Σradiated_power_controlled)) [dB]			
	4.8	2.8	4.6

Abbreviations: acc., acceleration; inc., incident; rad., radiating; lsp., loudspeaker, and inf., infinity.

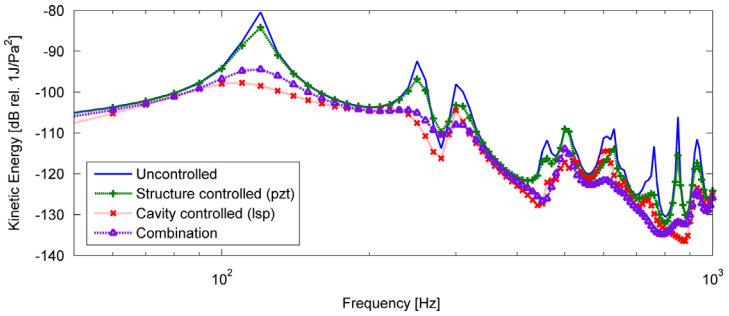

Fig. 16. Simulated kinetic energy response of the radiating panel with various control methods.

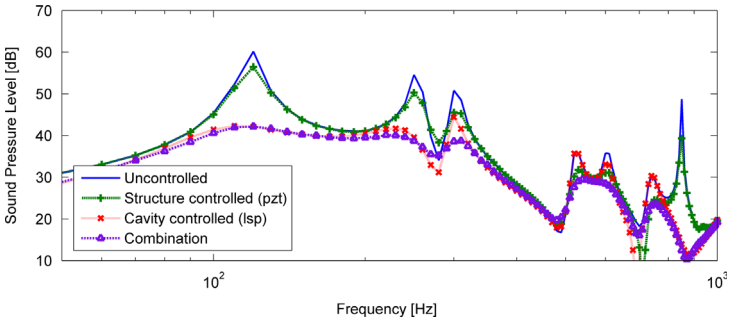

Fig. 17. Simulated SPL response above the radiating panel with various control methods.

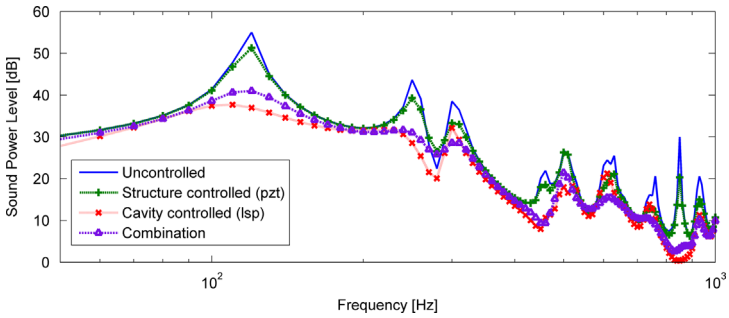

Fig. 18. Simulated SWL response of the radiating panel with various control methods.

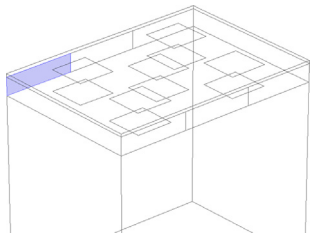

Fig. 19. Cavity control source configuration.

5. Comparison of cavity control strategies

From the previous comparison, we find that cavity control can provide significant noise reduction. Therefore, we present further investigations of various cavity sources in this section. Three types of cavity control sources are introduced, and the control performances are compared. The first type is a dynamic loudspeaker source, which operates as an acceleration source above the resonance frequency. The second type is an incident pressure source. The third type is controlling the pressure at the cavity boundaries. These three cavity control methods are applied at the boundaries of the cavity. The location of a cavity control source, which can be modelled as an acceleration source, incident pressure source, or pressure-controlled boundary, is marked in blue in Fig. 19. There are six cavity control sources along the cavity sides. To detect the error signal, there is one microphone in front of each control source.

In our model, sound wave radiation and propagation is governed in the frequency domain by

$$\nabla p + \mathrm{j}\omega\rho\mathbf{v} = \mathbf{0}, \tag{6}$$

$$\nabla \cdot \mathbf{v} + \mathrm{j}\omega\kappa p = 0, \tag{7}$$

where ∇ is the gradient in Eq. (6); ∇ is the divergence in Eq. (7); p [Pa] is the pressure; ρ [kg m^{-3}] is the density of air; $\mathbf{v}$ [m s^{-1}] is the particle velocity and κ [Pa^{-1}] is the compressibility of air. Eq. (6) is the equation of Newton's Law, and Eq. (7) is based on mass conservation. The principles of these various cavity sources are provided in the following sections.

5.1. Acceleration source loudspeaker

A dynamic loudspeaker is the most common type of loudspeaker. It can be assumed to operate as an acceleration source above the resonance frequency [23]. To model this type of loudspeaker, we control the acceleration of the loudspeaker surface. According to Eq. (6), the acceleration can produce an acoustic pressure p to the system as follows:

$$-\mathbf{n} \cdot \nabla p = \rho \mathbf{n} \cdot \mathbf{a}, \tag{8}$$

in which $\mathbf{n}$ is the normal vector to the loudspeaker surface and $\mathbf{a} = \mathrm{j}\omega\mathbf{v}$ [m s^{-2}] is the acceleration of the loudspeaker surface. The acoustic source impedance of the loudspeaker is assumed to be infinite.

5.2. Incident pressure source loudspeaker

The incident pressure source loudspeaker is used to produce a pressure source with a non-reflecting source boundary. A non-reflecting boundary condition (NRBC) equation, derived by Givoli and Neta, is applied to the model to introduce an incident pressure source into the system without reflections at the system's boundary [24]. This equation is based on a reformulation of the Higdon Non-Reflecting Boundary Condition [25,26]. The Higdon NRBC relies on a series of linear partial differential equations. By adjusting the parameters of the boundary condition, the reflection coefficient can be reduced to

zero for a certain incident angle. A higher order of the Higdon NRBC provides more incident angles that can be perfectly absorbed. Thus, less reflection is produced by the boundary. However, the order of the Higdon NRBC is limited in practical application because of computational difficulty. The Higdon NRBC orders and angles must be chosen based on experience to optimise the overall performance. The NRBC derived by Givoli and Neta uses additional auxiliary variables on the boundary to enable using the original Higdon NRBC up to any order. The second-order Givoli and Neta NRBC in the frequency domain is defined by

$$\mathbf{n}\cdot\nabla p+\mathrm{j}kp+\frac{\mathrm{j}\nabla^2 p}{2k}=\mathbf{n}\cdot\nabla p_i+\mathrm{j}kp_i+\frac{\mathrm{j}\nabla^2 p_i}{2k}, \tag{9}$$

where ∇^2 is the Laplacian and k is the wave number. The pressure p at the boundary can be derived if the incident pressure source p_i [Pa] is known. Furthermore, this equation can present the interactions in near-real conditions without any derivatives beyond the second order. An example of this incident pressure source is shown in Fig. 20. The right side of Fig. 20(a) acts as an incident pressure source loudspeaker with p_i. In addition, a point source is present in the centre. With these two sources, the pressure at the boundary (the right side of Fig. 20(a)) varies as the sum of these two pressure waves. Fig. 20(b) is the pressure distribution along the right side of Fig. 20(a), where the x-axis is the pressure value and the y-axis is the position along this boundary. It can be observed that the pressure varies along the boundary.

5.3. Pressure-controlled source loudspeaker

The third cavity control source is referred to as a pressure-controlled source loudspeaker. This cavity source controls the pressure at the boundary, which is the surface of the loudspeaker. The pressure p at the boundary is controlled as our control pressure value p_c [Pa]:

$$p=p_c. \tag{10}$$

An example of this pressure-controlled source loudspeaker is shown in Fig. 21. The right side of Fig. 21(a) acts as a pressure-controlled source loudspeaker with $p=p_0$. In addition, a point source is present in the centre. With the pressure-controlled source loudspeaker, the pressure at the controlled boundary (the right side of Fig. 21(a)) is maintained as the design value p_0, as shown in Fig. 21(b), where the x-axis is the pressure value and the y-axis is the position along this boundary.

5.4. Control performance comparisons

The noise reductions of these three cavity control sources are presented in three plots: the kinetic energy of the radiating panel, the sound pressure level at 10 cm above the radiating panel and the radiating sound power level of the structure (Figs. 22–24). The comparison is based on identical stability indexes (Table 9). The result shows that the pressure-controlled source loudspeaker can effectively reduce the broadband kinetic energy, but it increases the energy at certain frequencies, such as 600 Hz. In contrast, the incident pressure source loudspeaker does not increase the energy at any frequency below 1000 Hz. Therefore, the broadband reduction of the kinetic energy is higher than it is for the other two source types, being

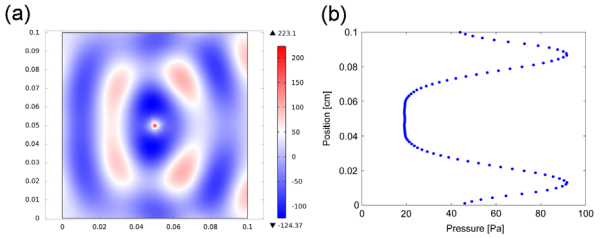

Fig. 20. Incident pressure source illustration: (a) pressure distribution; (b) pressure along the boundary.

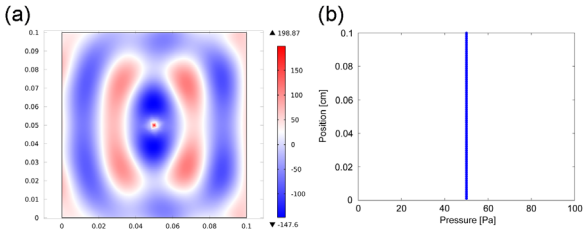

Fig. 21. Pressure-controlled source illustration (a) pressure distribution; (b) pressure along the boundary.

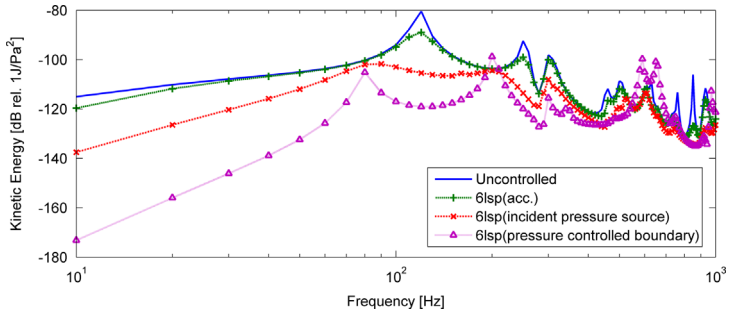

Fig. 22. Simulated kinetic energy response of the radiating panel with various cavity control sources.

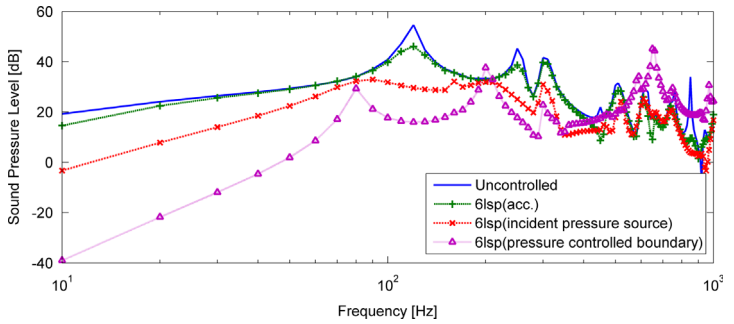

Fig. 23. Simulated SPL response above the radiating panel with various cavity control sources.

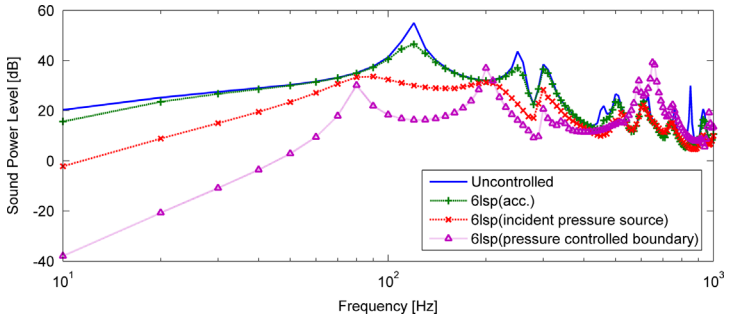

Fig. 24. Simulated SWL energy response of the radiating panel with various cavity control sources.

Table 9
Numerical analysis of stabilities, kinetic energy reduction and radiated sound power reduction from 10 to 1000 Hz.

Loudspeaker type	Acceleration source	Incident pressure source	Pressure-controlled source
Control gain	0.00042	0.2	0.029
Gain stability index	Inf.	34.6	Inf.
Phase stability index	58.7	59.8	59.8
Modulus stability index	0.87	0.62	0.75
Phase crossover frequency [10–20,000 Hz]	10,033	2187	6360
Total kinetic energy reduction (10*log 10(ΣKE_uncontrolled/ΣKE_controlled)) [dB]			
	4.9	13.3	13.2
Total radiated sound power reduction (10*log 10(Σradiated_power_uncontrolled/Σradiated_power_controlled)) [dB]			
	4.8	13.2	11.7

13.3 dB. This incident pressure source uses a non-reflecting boundary, which means that the energy can be propagated outside the cavity. Although there are no practical loudspeakers that use this source, an incident pressure source loudspeaker can be created using a dynamic loudspeaker, a microphone, and a velocity sensor with a feedback control loop.

6. Conclusions

Various control configurations for reducing the transmitted sound through a double panel structure have been studied in this paper. A structural–acoustic coupled FEM model, which can accurately predict the interactions between the structure vibration and acoustic wave propagation, has been developed. The investigations in this paper explain the difficulty of reducing noise by only controlling the radiating panel in a double panel structure. Numerical analysis showed that with direct velocity feedback control, piezoelectric actuators should be simultaneously applied to the incident panel and radiating panel in a double panel structure. This strategy is required because the resonant energy in a double panel structure is not only determined by the radiating panel but also by the incident panel and cavity. Therefore, the structural control should be applied to both panels. However, the interaction between the two panels reduces the control stability and limits the control performance. Moreover, structural control can barely reduce the resonant energy, which is dominated by the cavity resonance. Similar conclusions have been obtained from experimental results.

To further improve the control performance, various combinations of structural control methods and cavity control methods have been numerically studied and compared. To maintain fairness, the comparison was based on identical control stability indexes. The analysis has shown that cavity control can provide more noise reduction than structural control. Therefore, three types of cavity control sources were compared: the acceleration source loudspeaker, incident pressure source loudspeaker, and pressure-controlled source loudspeaker. The comparison has shown that the incident pressure source loudspeaker can achieve the largest total kinetic energy decrease of 13.3 dB and the largest total radiated sound power decrease of 13.2 dB within the frequency range from 10 Hz to 1000 Hz. This incident pressure source loudspeaker can be realised by using a dynamic loudspeaker, a microphone, and a velocity sensor with a feedback control loop.

Acknowledgements

This work was supported by STW (De Stichting voor de Technische Wetenschappen, The Foundation for Technical Sciences), Project no. 10602 IMPEDANCE (Integrated Modules for Power Efficient Distributed Active Noise Cancelling Electronics). The experimental development was supported by Henny Kuipers and Geert Jan Laanstra of the Signals and Systems Group, Faculty of EEMCS, University of Twente.

References

[1] Q. Mao, S. Pietrzko, Experimental study for control of sound transmission through double glazed window using optimally tuned Helmholtz resonators, *Applied Acoustics* 71 (2010) 32–38.
[2] C. Hirunyapruk, M.J. Brennan, B.R. Mace, W.H. Li, A tunable magneto-rheological fluid-filled beam-like vibration absorber, *Smart Materials and Structures* 19 (2010) 055020. (10 pp).
[3] F. Fahy, J. Walker, *Fundamentals of Noise and Vibration*, Routledge, New York, 1998.
[4] F. Fahy, P. Gardonio, *Sound and Structural Vibration: Radiation, Transmission and Response*, Academic Press, Elsevier, London, 2007.
[5] O.E. Kaiser, S.J. Pietrzko, M. Morari, Feedback control of sound transmission through a double glazed window, *Journal of Sound and Vibration* 263 (2003) 775–795.
[6] J. Pan, C. Bao, Analytical study of different approaches for active control of sound transmission through double walls, *Journal of the Acoustical Society of America* 103 (1998) 1916–1922.
[7] J.P. Carneal, C.R. Fuller, An analytical and experimental investigation of active structural acoustic control of noise transmission through double panel systems, *Journal of Sound and Vibration* 272 (2004) 749–771.
[8] P. Gardonio, E. Bianchi, S.J. Elliott, Smart panel with multiple decentralized units for the control of sound transmission. Part I: theoretical predictions, *Journal of Sound and Vibration* 274 (2004) 163–192.
[9] P. Gardonio, E. Bianchi, S.J. Elliott, Smart panel with multiple decentralized units for the control of sound transmission. Part II: design of the decentralized control units, *Journal of Sound and Vibration* 274 (2004) 193–213.
[10] P. Gardonio, E. Bianchi, S.J. Elliott, Smart panel with multiple decentralized units for the control of sound transmission. Part III: control system implementation, *Journal of Sound and Vibration* 274 (2004) 215–232.
[11] A.P. Berkhoff, J.M. Wesselink, Combined MIMO adaptive and decentralized controllers for broadband active noise and vibration control, *Mechanical Systems and Signal Processing* 25 (2011) 1702–1714.
[12] P.A. Nelson, S.J. Elliott, *Active Control of Sound*, Academic Press, London, 1992.
[13] S.J. Elliott, P. Gardonio, T.C. Sors, M.J. Brennan, Active vibroacoustic control with multiple local feedback loops, *Journal of the Acoustical Society of America* 111 (2002) 908–915.
[14] N. Alujevic, P. Gardonio, K.D. Frampton, Smart double panel with decentralized active dampers for sound transmission control, *AIAA Journal* 46 (2008) 1463–1475.
[15] N. Alujevic, P. Gardonio, K.D. Frampton, Smart double panel for the sound radiation control: blended velocity feedback, *American Institute of Aeronautics and Astronautics Journal* 49 (2011) 1123–1134.
[16] S.J. Pietrzko, Q. Mao, New results in active and passive control of sound transmission through double wall structures, *Aerospace Science and Technology* 12 (2008) 42–53.
[17] A.P. Berkhoff, Piezoelectric sensor configuration for active structural acoustic control, *Journal of Sound and Vibration* 246 (2001) 175–183.
[18] M.J. Balas, Direct velocity feedback control of large space structures, *Journal of Guidance, Control, and Dynamics* 2 (1979) 252–253.
[19] S. Skogestad, I. Postlethwaite, *Multivariable Feedback Control: Analysis and Design*, John Wiley & Sons, Chichester, 1996.
[20] P. Gardonio, N. Alujevic, Double panel with skyhook active damping control units for control of sound radiation, *Journal of the Acoustical Society of America* 128 (2010) 1108–1117.
[21] M.E. Johnson, S.J. Elliott, Active control of sound radiation using volume velocity cancellation, *Journal of the Acoustical Society of America* 98 (1995) 2174–2186.
[22] A. Preumont, *Vibration Control of Active Structures*, Kluwer Academic Publishers, London, 2004.
[23] M. Rossi, *Acoustics and Electroacoustics*, Artech House, Norwood, MA, 1988.
[24] D. Givoli, B. Neta, High-order non-reflecting boundary scheme for time-dependent waves, *Journal of Computational Physics* 186 (2003) 24–46.
[25] R.L. Higdon, Absorbing boundary conditions for difference approximations to the multi-dimensional wave equation, *Mathematics of Computation* 47 (1986) 437–459.
[26] R.L. Higdon, Numerical absorbing boundary conditions for the wave equation, *Mathematics of Computation* 49 (1987) 65–90.